AGU ADVANCING EARTH AND SPACE SCIENCE

Earth and Space Science

RESEARCH ARTICLE
10.1029/2021EA002093

Seismic and Electrical Geophysical Characterization of an Incipient Coastal Open-System Pingo: Lagoon Pingo, Svalbard

Craig P. Hammock[1,2,3], Bernd Kulessa[1,4], John F. Hiemstra[1], Andrew J. Hodson[3,5], and Alun Hubbard[2,6]

[1]Department of Geography, College of Science, Swansea University, Swansea, UK, [2]Department of Geosciences, Centre for Arctic Gas Hydrate, Environment and Climate, UiT–The Arctic University of Norway, Tromsø, Norway, [3]Department of Arctic Geology, University Centre in Svalbard (UNIS), Longyearbyen, Norway, [4]School of Technology, Environments and Design, University of Tasmania, Hobart, TAS, Australia, [5]Department of Environmental Science, Western Norway University of Applied Sciences, Sogndal, Norway, [6]Department of Geography, University of Oulu, Oulu, Finland

Abstract Whilst there has been a recent appreciation for the role of open-system pingos in providing a fluid-flow conduit through continuous permafrost that enables methane release, the formation and internal structure of these ubiquitous permafrost-diagnostic landforms remains unclear. Here, we combine active-source seismic measurements with electrical resistivity tomography to investigate the structural and subsurface characteristics of an incipient open-system pingo actively emitting methane within the glacio-isostatically uplifting fjord valley of Adventdalen, Svalbard. Wavefront inversion of seismic refractions delineate a spatially heterogeneous active layer, whilst deeper reflections identify the lithological boundaries between marine sediments and underlying shales at ~68 m depth (p-wave velocity of ~1,790 ms^{-1}). Low geometric mean inverted resistivities of 40–150 Ωm highlight the dominance of saline permafrost, whilst elevated resistivities (~2 kΩm) occur close to the groundwater spring and in heaved areas around the pingo. Based on our results, we speculate that segregation ice dominates the pingo structure, given the absence of a notable resistivity contrast characteristic of injection ice that is typically expected within early open-system pingo formation, and provides the most plausible geomorphic agent within the local fine-grained sedimentology. Our results thereby indicate that sediment grain size and moisture availability can provide important controls on pingo formation. This study shows that open-system pingos in coastal, saline permafrost environments may form differently, with implications for localized permafrost structure, its permeability to underlying gas reservoirs and consequent methane release.

Plain Language Summary Considerable amounts of methane, a potent greenhouse gas, can flow through ground which is permanently below freezing (permafrost) through dome-shaped landforms called open-system pingos. These landforms occur in the lowlands of mountainous cold regions, from water under pressure from deep underground. However, the formation and internal structure of these landforms are unclear. We use geophysical techniques involving seismic waves and electrical resistivity to characterize the internal structure of a young pingo in Svalbard. Our seismic investigation find a seasonally thawing (active) layer with a variable thickness, and a deeper reflection at ~68 m which we interpret as the boundary between marine sediments and bedrock. Meanwhile, relatively low electrical resistivities indicate that the ground is saline, and suggest an internal structure that is dominated by discrete layers of ice known as segregated ice, as opposed to a large body of ice which is ordinarily expected. Our results indicate that sediment grain size and moisture availability are important controls on pingo formation. This is important as there may be differences in how these pingos form, and this will impact the structure of local frozen ground and in how they allow the escape of methane stored deep beneath the permafrost.

Key Points:

- Seismic refraction, reflection and electrical resistivity tomography are used to characterize a coastal methane-emitting incipient pingo
- Low resistivities and geomorphology preclude massive ice presence, and indicate segregation ice dominates early pingo internal structure
- Sedimentology and moisture availability are critical controls on early pingo formation, and causes plurality within pingo structures

Supporting Information:

Supporting Information may be found in the online version of this article.

Correspondence to:

C. P. Hammock,
786421@swansea.ac.uk

Citation:

Hammock, C. P., Kulessa, B., Hiemstra, J. F., Hodson, A. J., & Hubbard, A. (2021). Seismic and electrical geophysical characterization of an incipient coastal open-system pingo: Lagoon Pingo, Svalbard. *Earth and Space Science*, *9*, e2021EA002093. https://doi.org/10.1029/2021EA002093

Received 26 OCT 2021
Accepted 20 DEC 2021

Author Contributions:

Conceptualization: Craig P. Hammock, Bernd Kulessa, John F. Hiemstra, Andrew J. Hodson, Alun Hubbard
Formal analysis: Craig P. Hammock, Bernd Kulessa
Funding acquisition: Craig P. Hammock, Bernd Kulessa, John F. Hiemstra, Alun Hubbard
Investigation: Craig P. Hammock, Bernd Kulessa
Methodology: Craig P. Hammock, Bernd Kulessa

1. Introduction

The ongoing degradation of Arctic permafrost is potentially one of the most significant, yet poorly understood consequences of amplified climate warming. The possible release of vast inventories of sequestered carbon as potent greenhouse gases is considered one of the most serious threats in future acceleration of warming (Nisbet et al., 2016; Pithan & Mauritsen, 2014). Processes including the desiccation and decomposition of carbon-rich soils and peatlands (Koven et al., 2011; Lawrence et al., 2015), the abrupt thaw of ground ice (Turetsky et al., 2019, 2020) and ebullition through lakes (Walter Anthony et al., 2012) are ongoing contributors to

Supervision: Bernd Kulessa, John F. Hiemstra, Andrew J. Hodson, Alun Hubbard
Writing – original draft: Craig P. Hammock
Writing – review & editing: Craig P. Hammock, Bernd Kulessa, John F. Hiemstra, Andrew J. Hodson, Alun Hubbard

atmospheric methane. Moreover, natural gas trapped across the subsurface in either free form or gas-hydrates can be released in potentially massive quantities as the overlying impermeable permafrost cap degrades.

Our ability to model and understand future greenhouse gas emissions from permafrost environments relies heavily on knowledge of emission processes, and particularly on being able to predict the way ground ice might disintegrate. It is well-known that changing thermokarst landscapes (Turetsky et al., 2020) and vegetation patterns (Grünberg et al., 2020; Loranty et al., 2018) modulate thermal conditions in the ground, leading to significant localized differences in both extent and thickness of the permafrost. Geological and geomorphological processes and features also provide controls on the continuity and configuration of ground ice. Varying sediment properties (e.g., Lawrence et al., 2008) and geologic structures (Mishra et al., 2021) could lead to differences in thermal and hydrological properties and consequently to heterogeneities in the permafrost layer.

Among the hetereogeneities within continuous permafrost environments are open-system pingos; permafrost-diagnostic mound-like landforms that are typically up to 40 m in height and 100–500 m across (Ballantyne, 2018; Harris et al., 2017). Open-system pingos are widely considered to form following the artesian injection of hydraulically pressurized groundwaters (Müller, 1959), recharged through the temperate zones of glaciers (Liestøl, 1977) into the near-surface. It is typically believed that initial pingo formation occurs following the freezing of injected groundwaters into massive ice lenses (also referred to as "injection ice"; Mackay, 1973), resulting in a characteristic, dome-shaped landform. However, whilst it is proposed that initial pingo growth occurs solely from injection ice (French, 2007), this would require the balance of water pressures, overburden strength and freezing rates, which vary naturally. Consequently, ice segregation, whereby porewater migration towards the freezing plane produces discrete ice lenses within the soils, is suggested to occur following initial pingo growth (French, 2007; Mackay, 1973), although more recent studies have questioned whether this dominates their geomorphology (Kunz & Kneisel, 2021; Ross et al., 2007). In addressing the distribution of open-system pingos, Yoshikawa and Harada (1995) suggest three groupings: (a) those formed whereby groundwaters exploit existing geologic faults and structures; (b) those which occur in areas of artesian flow as a consequence of subglacial meltwaters (cf. Liestøl, 1977) and, (c) those occurring in nearshore or low-lying environments, undergoing glacio-isostatic uplift. Despite this categorization of their hydraulic properties, the mechanism and processes which govern pingo formation still remain poorly understood (Demidov et al., 2019; Gurney, 1998; Kunz & Kneisel, 2021), and studies assessing early pingo forms remain limited.

This need for detailed information on the internal structures and genesis of open-system pingos has been emphasized by recent studies highlighting significant methane emissions from these landforms (Hodson et al., 2019, 2020), and the need for an understanding of ground-ice distributions given risk of permafrost thaw (Turetsky et al., 2019). As open-system pingo formation is inherently linked to groundwater flow through permafrost, their role in providing a flow conduit through which deeply seated methane migrates has come under increased scrutiny (Hodson et al., 2019, 2020). The significance of open-system pingos enabling methane release has been shown in emissions estimates from Lagoon Pingo in Adventdalen, Svalbard, whereby Hodson et al. (2019) suggests year-round methane release of ~64 kg CH4 a^{-1}, by diffusion alone, exceeding that of wetland emission estimates when normalized for surface area (Pirk et al., 2017). Methane emissions have indeed been found at four of the five pingos in Adventdalen (Hodson et al., 2020). In essence, it has been suggested that these landforms are terrestrially analogous to submarine pockmarks and gas seep forms, which have been extensively studied on the Barents Sea Shelf (Andreassen et al., 2017; Portnov et al., 2013; Serov et al., 2017). Critically, unlike submarine forms where escaping methane is oxidized within the water-column, terrestrial open-system pingos release gas that directly contributes to the atmospheric carbon budget.

Here, we use a combination of active-source seismic and electrical resistivity tomography (ERT) techniques to characterize the internal structures of Lagoon Pingo, in Adventdalen, Svalbard. This coastal, incipient open-system pingo, represents the youngest in a chain of five formed from Holocene glacio-isostatic uplift, and was specifically selected because of its documented methane release (Hodson et al., 2019, 2020). We hypothesize that the geomorphology is dictated by lenses of massive, injected ice (Mackay, 1973), forming as a consequence of the near-surface freezing of groundwater upwelling, and that the present-day springs flow around these lenses to the surface. We test this notion by constraining the near-surface structure of Lagoon Pingo to understand the genesis of open-system pingo forms, and assess how these interact with groundwater springs and associated methane release.

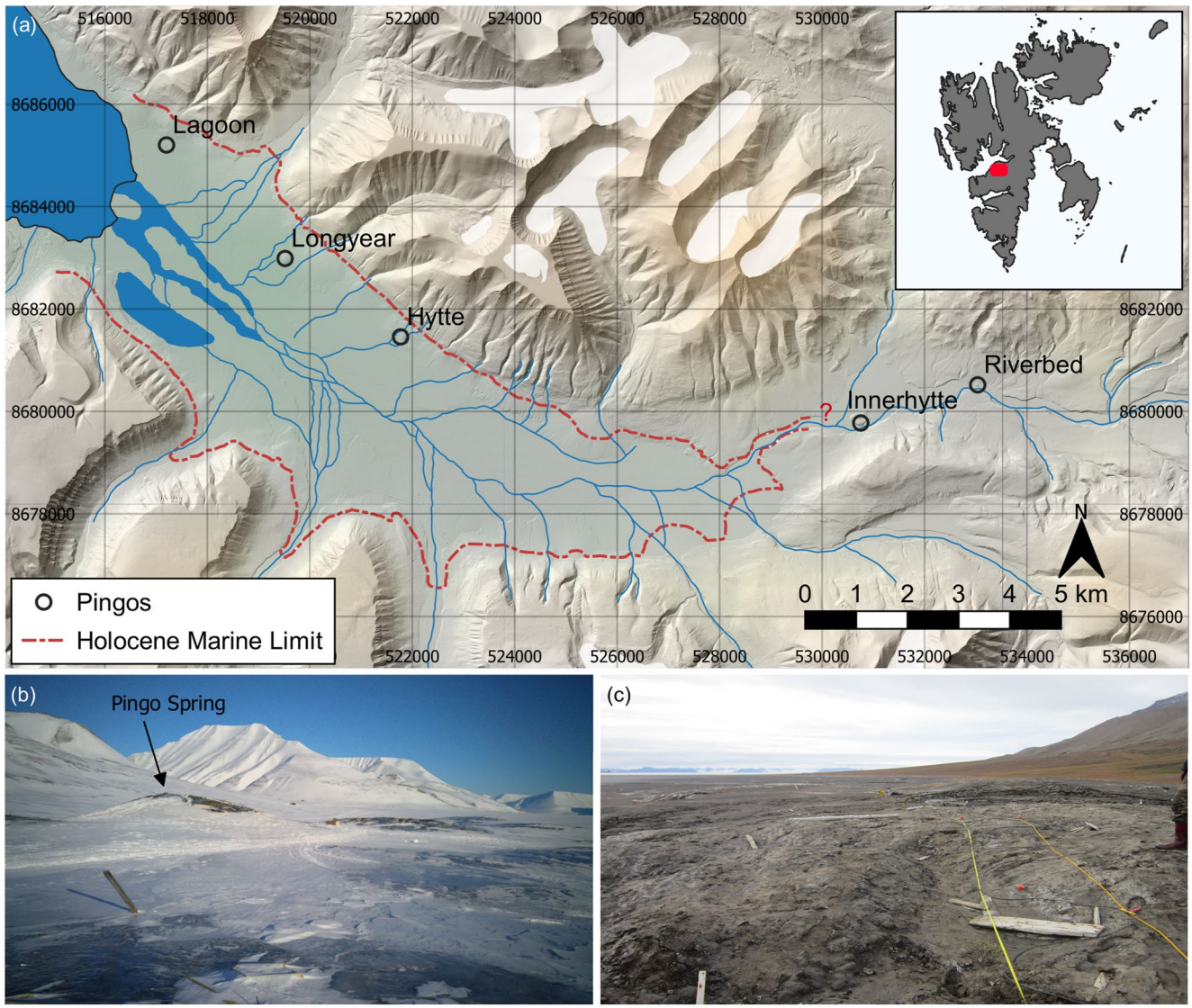

Figure 1. (a) The location of pingos in Adventdalen and the approximate extent of the Holocene marine transgression. Topography is depicted using a 5 m-resolution 2010 DEM (Norwegian Polar Institute, 2014). Coordinates are shown in UTM 33N. (b) View facing northeast depicting the center of the Lagoon Pingo site during winter. (c) View facing northwest of the Lagoon Pingo spring during summer.

2. Field Site and Methods

2.1. Field Site

Lagoon Pingo (location shown in Figure 1) is the westernmost in a chain of five open-system pingos located in Adventdalen, Svalbard. Lagoon Pingo is located close to the contemporary coastline on the edge of a saltwater lagoon, which is protected from regular tides by a beach ridge. However, significant driftwood accumulated on the coastal side of the pingo suggests susceptibility to exceptional tides and storms. Lagoon Pingo has a chaotic topography dissimilar to the dome-shaped mound typical of other open-system pingos in Svalbard, and consists of a series of mud/clay mounds spanning 500 m in length and 200 m in width, and ~8 m tall at its highest point. The pingo is fed by two perennial groundwater springs that emerge at the surface, forming extensive protruding icings during freezing winter conditions and small ponds in the summer. Following Liestøl (1977), these springs occur as a consequence of high artesian pressures in the underlying aquifers, which are most likely continually recharged by the percolation of waters through the temperate zones of nearby glaciers.

The genesis of Lagoon Pingo as a terrestrial open-system pingo is consistent with the rapid sedimentation and isostatic-uplift of the glacially cut fjord valley in which it is located. Adventdalen is a steep-sided valley glacially eroded into Early Cretaceous and Palaeogene sedimentary sandstones and shales (Gilbert et al., 2018; Major et al., 2001). Following retreat of the Barents Sea Ice Sheet which covered much of the Barents Shelf and western Svalbard at the last glacial maximum (c. 20 ka) to complete deglaciation at c. 10 ka, Adventdalen has been undergoing rapid relative sea level fall as a result of a high rate of glacio-isostatic rebound (3.7 $mmyr^{-1}$; Auriac et al., 2016) surpassing eustatic rise. Consequently, the present-day Holocene marine limit persists at 62–70 m above current sea level (Lønne & Nemec, 2004), with rapid rates of glaciomarine and aeolian sedimentation. These lead to the current morphology of Adventdalen as a wide-bottomed, infilled fjord valley, fed by fluvioglacial sediments from a seasonal braided river system through the center. Permafrost is prevalent and laterally continuous (Christiansen et al., 2010; Humlum et al., 2003), with general estimates of permafrost thickness ranging from 100 m at the valley bottom to 300–400 m at higher altitudes (Humlum, 2005). The aggradation of permafrost following deglaciation forms a fundamental agent of pingo formation, and is a potential driver of groundwater to the surface (Hornum et al., 2020).

The three topographically lower/western-most open-system pingos are situated in marine sediments within Adventdalen and are proposed to represent different stages of pingo evolution, from initiation (Lagoon Pingo) to maturity (Longyear Pingo), and pingo reactivation following decline (Hytte Pingo) (Yoshikawa & Harada, 1995). This follows radiocarbon dates obtained from peat sediments and mollusc shells on these pingos, whereby Lagoon Pingo is suggested to be 140 ± 20 years BP (Yoshikawa & Nakamura, 1996), in contrast to older dates of 2,800 ± 90 years BP and 6,980 ± 70 years BP for Longyear and Hytte Pingo, respectively. Each of these pingos are sited alongside the northern flank of the valley, and whilst Hytte Pingo coincides with a geological boundary (e.g., Hornum et al., 2021), no known faults or geological boundary crosses the Lagoon Pingo site. Despite this, local alluvial fans may extend beneath the pingos and provide intrusions of coarser sediments that enhance hydraulic conductivity.

While recent studies have examined seasonal hydrology and gas emission dynamics at Lagoon Pingo (Hodson et al., 2019), geophysical investigation has been limited to summer electrical resistivity surveys and borehole sampling (Harada & Yoshikawa, 1996; Yoshikawa & Harada, 1995). They describe a low resistivity (1.1 Ω.m), shallow (0.8 m) surface layer, interpreted as the seasonally unfrozen active layer, above a deeper (~22.8 m), extensive permafrost layer with resistivities of at least an order of magnitude greater. The deepest layer was characterized by low resistivities similar to the active layer, with borehole validation confirming a transition from frozen to unfrozen sediments. In contrast, the other open-system pingos within Svalbard have been more extensively studied. In ERT measurements of Innerhytta Pingo close to the marine limit, Ross et al. (2007) suggest high resistivities of 10–30 kΩ m, indicating a high proportion of ice, if not massive ice. In seismic investigations of Innerhytta Pingo, Rossi et al. (2018) described a 15 m thick surface layer with a P-wave velocity of ~4–5 km s^{-1} as frozen permafrost, which overlay a lower P-wave velocity zone (~2 km s^{-1}) interpreted as partially unfrozen sediments hosting the groundwater circulation controlling the pingo spring. At Hytte and Longyear Pingo, saline permafrost was determined to have resulted in frozen sediments with resistivity below <2 kΩ m (Ross et al., 2007). Additionally, valley-scale surface nuclear magnetic resonance and controlled source audio-magnetotellurics have demonstrated lateral variability in liquid water content within the permafrost, with up to ~10% liquid water near to the coast suggesting the persistence of cryopegs beneath Adventdalen that permit further intrapermafrost groundwater mobility (Keating et al., 2018).

2.2. Methods

2.2.1. Seismic Investigations

Active source seismic investigations are well established in geomorphological studies (Schrott & Sass, 2008). Seismic methods are based upon the principle that elastic waves travel through different subsurface media at different velocities, with this dependent upon composition and material density. By measuring the elapsed time between the triggering of a quantified seismic signal, and its return following refraction or reflection from a subsurface change in acoustic impedance, a non-intrusive interpretation of subsurface properties can be obtained. Further detail can be established through an understanding of the polarity and amplitude of the obtained seismic returns, should data quality permit.

The use of seismic methods within permafrost environments is highly dependent upon sharp increases in P-wave velocity where media is frozen (Zimmermann & King, 1986). Consequently, seismic refraction and reflection methods are commonly used in the detection of permafrost extent (Schrott & Hoffmann, 2008). For example, seismic refraction methods are often used to determine active layer depth, given that the P-wave velocities of the active layer (400–1,500 ms^{-1}) and frozen permafrost (2,000–4,000 ms^{-1}) show sufficient contrast (Hauck & Vonder Mühll, 2003; Hauck et al., 2007). Notably however, refraction methods are limited in requiring velocities to increase with depth. In permafrost environments, whereby frozen layers often exhibit increased P-wave velocity, this inhibits the detection of the permafrost base. Seismic reflection methods are often used to obtain interfaces deeper within the subsurface, and have been utilized within permafrost and periglacial environments to determine the depth of the permafrost base (Schwamborn et al., 2002).

2.2.2. Electrical Resistivity Tomography (ERT)

ERT utilizes differences in the ability of materials to resist the flow of an electrical current to establish bulk electrical resistivity contrasts within the subsurface. These bulk resistivity characteristics are controlled by different mechanisms that enable the flow (e.g., conduction, the reciprocal of insulation) of electrical current through media: particle conduction, surface conduction and ionic (or electrolytic) conduction. Particle conduction relates to conductivity caused by a high number of free electrons, often within metallic materials. Surface conduction occurs through the electrical double layer at the interface between particle and fluid, which is controlled by pore-water content and the electrical properties of the media (e.g., cation exchange capacity, zeta-potential). Lastly, ionic (otherwise known as electrolytic) conduction refers to that caused by the transit of ions through media, normally resulting from liquid flow. As a consequence, ionic conduction is typically controlled by the porosity, saturation, pore connectivity, and fluid conductivity of a material (Mollaret et al., 2019). These three mechanisms determine the bulk conductivity, and thus the bulk resistivity, of a given medium.

ERT is commonly applied to establish soil properties (e.g., lithology, porosity, structural characteristics, and pore fluids), stratigraphy and heterogeneities within a given subsurface (Klein & Santamarina, 2003). In permafrost environments, the differences in conduction between electrically conductive liquid water and resistive ice render ERT an effective method for the identification and interpretation of frozen and unfrozen sediments, with typical applications including the identification of active layer depths (e.g., Kasprzak, 2015; Léger et al., 2017), the permafrost base (Sjöberg et al., 2015; You et al., 2013) and in the detection of ground ice (Hauck & Vonder Mühll, 2003). However, whilst frozen pore water content typically increases electrical resistivity by several orders of magnitude, exceptions can occur in marine sediments where pore waters are conductive and surface conduction mechanisms exist at the particle-ice-water interfaces within the pore spaces (e.g., Revil & Glover, 1998).

2.3. Data Acquisition

2.3.1. Seismic Investigations

Active source seismic data were acquired in August 2019 across two profiles which together cover the length of the pingo complex. The data were acquired using two Geometrics Geode 24 Channel seismographs, with profiles consisting of 48 100 Hz geophones deployed at 4 m spacings. Shots were made using a sledgehammer source on a metal baseplate at 4 m intervals midway between geophones and up to 10 m off-end, with additional shots taken every 10 m up to a distance of 50 m from the end of the profile. A set of 10 shots were taken per shotpoint in order to allow stacking, with each profile therefore containing 610 shots in total.

Processing of the seismic reflection data was completed in REFLEXW version 9.5 (Sandmeier, 2020). Whilst planimetric positions of shotpoints and geophones were obtained by tape measure, GPS positions of geophones were taken using a Garmin eTrex handheld GPS with horizontal accuracy of c. 5 meters, to obtain topography using a 2009 summer 5 m DEM (Norwegian Polar Institute, 2014). Traces that were visibly noisy or dead were manually removed from shotgathers prior to stacking. To analyze seismic reflections across the site, a common midpoint gather was produced using the 4 m-spaced shots by resorting and stacking traces according to their offset. The velocity of identified hyperbolae were then obtained through manual curve-fitting within REFLEXW. An initial estimation of the internal velocity was obtained through Dix's formula (Dix, 1955) to form a preliminary model, although it is noted that this does not satisfy the assumptions of standard NMO velocity analysis (Bradford, 2002). Consequently, we use this model following the recommendations of Bradford and Sawyer (2002), by applying this estimation on unstacked data through a pre-stack depth migration. Unstacked

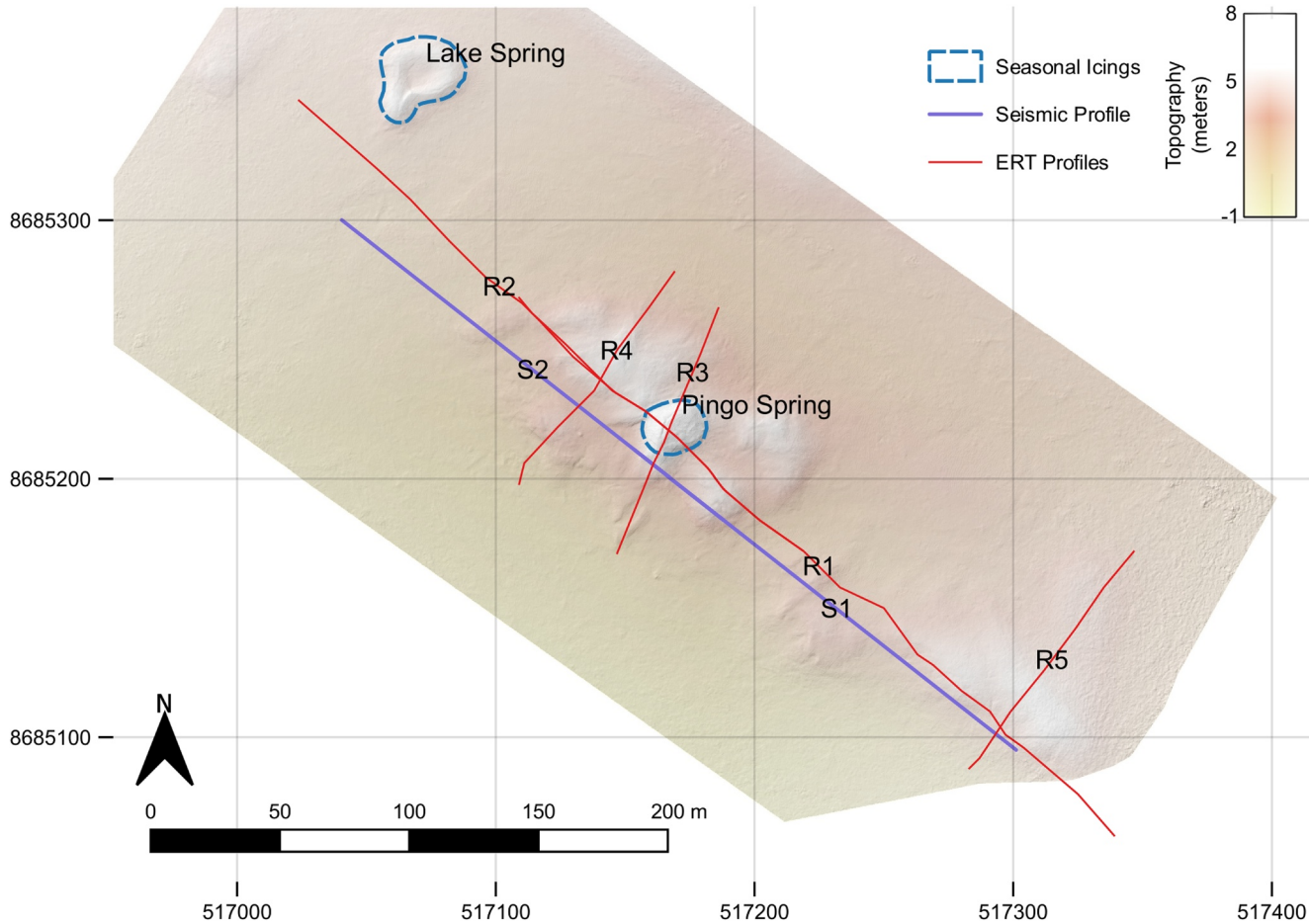

Figure 2. Locations of profiles over the Lagoon Pingo site, depicted on a sub-meter DEM derived using Structure-from-Motion in April 2020 (Hann & Dachauer, 2020). Co-ordinates shown are UTM 33N.

data were processed by applying a manual gain adjustment (to enhance signal with depth) and bandpass filtering (to minimize surface waves), followed by resampling at 3 ms due to processing constraints, and finally a pre-stack depth migration using Kirchhoff weighted factors for the summation of raypaths.

To analyze seismic refractions, first onsets were manually picked for each shotpoint. Following traveltime analysis as per standard procedure in REFLEXW (Sandmeier, 2020), a two-layer wavefront inversion was subsequently conducted using the forward and reverse traveltimes, by utilizing a finite difference approximation of the eikonal equation which is analogous to the FD-vidale method used in forward raytracing (Sandmeier, 2020; Vidale, 1988, 1990). Seismic refraction tomography was conducted to provide a secondary analysis of the data, whereby the Simultaneous Inversion Reconstruction Algorithm (van der Sluis & van der Vorst, 1987) was used to automatically adapt synthetic data to observed travel times through calculation of the seismic P-wave ray paths. In accordance with initial wavefront inversion data, an initial model with a surface P-wave velocity of 375 ms^{-1}, increasing by 200 ms^{-1} with each meter in depth was used. The parameterization of the tomographic inversion is shown in the Table S1 in Supporting Information S1. Goodness of fit was assessed using forward raytracing through a finite difference calculation (Vidale, 1988, 1990).

2.3.2. Electrical Resistivity Tomography

A series of ERT profiles were collected in early April 2019 using an ABEM SAS1000 Terrameter, whilst the site remained frozen. Two profiles (R1 and R2 in Figure 2) were collected to encompass the NW-SE extent of the site, with each profile containing 53 stainless steel electrodes at a spacing of 5 m to cover full extent of 260 m. These profiles contained an overlap over central parts of the site to ensure suitable data coverage over the

Table 1
Number of Successful and Failed Measurements for Configurations Within Each Profile, With Rates of Excluded Measurements Following Further Pre-Processing

Profile	Total number of configurations	Successful measurements (normal and reciprocal)	Measurements following filtering
R1	443	388	206
R2	443	214	100
R3	63	61	52
R4	63	61	53
R5	63	63	61

primary upwelling and for error analysis. These profiles were supplemented by shorter, quasi-perpendicular transects containing 21 electrodes to cover a lateral extent of 100 m (R3-R5 in Figure 2). Wenner array configurations were used for each profile to provide the best compromise between vertical and horizontal resolution in an uncertain environment, given that contact resistance was high (Hauck & Vonder Mühll, 2003). Where electrodes occurred in snow-covered areas, snow pits were dug, and all electrodes were hammered in using a rubber mallet until firmly emplaced within the ground. To counteract electrode contact issues resulting from the high resistivity of frozen surfaces in sub-zero conditions, a saline solution was poured onto each electrode prior to each measurement, and snow pits were dug where required. Given the variable surface conditions, the instrument was set to select current automatically for each measurement within all profiles. For each profile, normal and reciprocal measurements were obtained. However, despite our best efforts, poor contact for a minority of electrodes resulted in failure to measure a potential for some electrode configurations, with success rates shown in Table 1. Configurations whereby either or both of the normal or reciprocal measurements failed were consequently excluded from further data processing.

The data were further pre-processed and inverted in ResIPy (see Blanchy et al., 2020); an open-source graphical user interface for the Occam's type R2 inversion algorithm (Binley & Kemna, 2005). First, data were filtered through comparisons of results obtained by normal and reciprocal measurements, with those that exceeded a 10% difference in apparent resistivities excluded. For some profiles, this resulted in the exclusion of a high proportion of measurements (shown in Table 1), largely pertaining to measurements occurring from particular electrodes (see Figure S3 in Supporting Information S1). To account for errors within measurements and to discretize the initial model, an error model was subsequently fit. This follows Koestel et al. (2008), where the assumption is that true error relates to both an absolute (a) and a relative component (b), which are used to determine data weightings and parameterize the final inversion model. To complete this, measurements were binned by their apparent resistivity into groups of ~20 and fit to an error model. For shorter profiles (R3–R5), a linear error function was used owing to the smaller number of measurements, given by:

$$\varepsilon = a + b\rho$$

where, ε is the standard deviation and ρ is the mean of each bin in Ohms. Constants a and b were then defined by the best linear fit. For longer profiles, a linear error model provided a poor fit for measurements which contained lower mean resistivities, and thus constants a and b were defined through the best fit of a power-law based error function where:

$$\varepsilon = b\rho^{a}$$

The inversions were discretized using a custom transfinite mesh, built around surface topography as defined by a decimeter-resolution DEM derived through Structure-from-Motion photogrammetry from a drone survey conducted in April 2020 (cf. Hann & Dachauer, 2020; Westoby et al., 2012). The horizontal resolution of the mesh foreground was defined by 2 cells per electrode, whilst the vertical cell size increased away from the surface where sensitivity to the input data was expected to be greatest. The foreground meshes were constrained by depth using a default 2/3 of the maximum dipole length, and the initial model resistivity was set to the geometric mean of apparent resistivity for each profile.

The inversion using the R2 algorithm involves a least squares weighted function (Blanchy et al., 2020), which aims to find the smoothest model that conforms to and remains consistent with the data. For each model, the weights were updated as the inversion progressed using a routine based on Morelli and LaBrecque (1996).

The inverted models were appraised for their reliability through multiple methods. Inversions were initially checked using normalised model error, as per Binley et al. (1995), to ensure that these fit within a ±3% threshold. Following this, the sensitivity of the inverted models to the initial data were checked using an accumulated sensitivity map (Binley & Kemna, 2005; Kemna, 2000; Park & Van, 1991), calculated through the evaluation of both

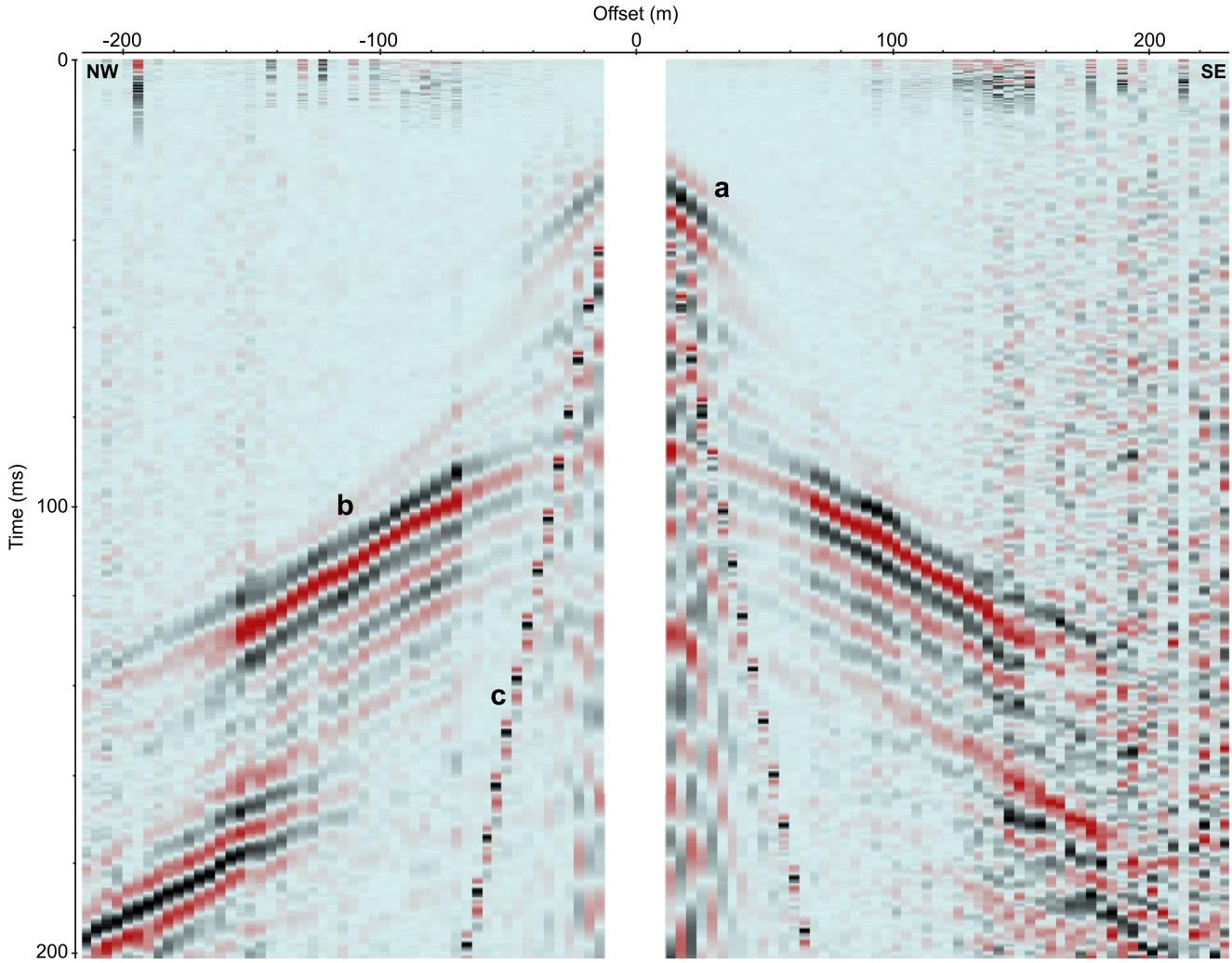

Figure 3. Common midpoint gather depicting homogeneous refractions and reflections from across Lagoon Pingo, shown without gain. Letters indicate (a) the near surface P-wave refraction from marine sediments, (b) P-wave reflection from the boundary between overlying marine sediments and underlying strata and (c) the direct air wave.

the Jacobian and data weighting matrix. A threshold of 0.001 x S_{max} was used to determine parts of the inversions which were deemed sensitive to the initial data (Kemna, 2000). This sensitivity matrix is presented with each resistivity profile below, and areas which are below this sensitivity threshold are shown as semi-transparent. Lastly, the reliability of separate inversions were tested by analysis of the correlation between profiles where these intersect (see Supporting Information S1).

3. Results

3.1. Seismic Reflection

The result of our seismic reflection investigations are shown by the common midpoint gather in Figure 3, whereby a hyperbolae beginning at ~80 ms at zero offset is the most apparent feature. This homogeneous reflector remains visible up to approximately 160 m from the shotpoint following geometric correction, and exhibits a P-wave velocity of ~1,787.1 ms^{-1} once corrected for the overlying active layer. A multiple of this can be seen at wide offsets, with this particularly clear where offset is negative due to noise obtained in the opposite direction. The only other reflection feature apparent is the air wave with a P-wave velocity of 330 ms^{-1}.

3.2. Seismic Refraction

In addition to deeper reflection features, a near-surface refraction is highlighted on the common midpoint gather (Figure 3) with a preliminary manual interpretation suggesting a shallow active layer with P-wave velocities of ~394 ms^{-1} above a deeper second layer with a V_p of 2,110 ms^{-1} (see Figure S1 in Supporting Information S1).

Figure 4 shows the wavefront inversion (red line), assuming that a two-layer model persists in the near-surface of the Lagoon Pingo site (as derived from the preliminary analysis of the common midpoint gather), and 2-D refraction tomography obtained from the first arrival picks of seismic data. The wavefront inversion identifies a lower velocity layer overlying a higher velocity layer within the immediate subsurface at the site, with depths consistent with analogous coastal sites elsewhere on Svalbard (e.g., Christiansen et al., 2020). The greatest depths occur in the northwestern part of the profile in a low-lying, flat section close to the lake spring, where values in excess of ~3 m are obtained. Whilst the wavefront inversion largely echoes the shape of the surface topography, the minimum layer depth of 1.1 m occurs within heaved sediments where the topography is most variable. Estimates of upper layer P-wave velocity from the wavefront inversion equal 385 ± 20.7 ms^{-1}, highlighting a homogeneous layer with a low P-wave velocity across the length of the profile.

In contrast, the seismic tomography model shows an increase in velocity with depth, but depictions of two distinct layers is ambiguous. Velocities of ~400 ms^{-1} at the surface increase to 600–700 ms^{-1} at a depth of 2–3 m due to the initial model used, and increase rapidly thereafter. Notably, the tomography depicts lateral variations in P-wave velocity below a depth of 5 m, with lower P-wave velocities at greater depths over flat, low-lying parts of the profile when compared to heaved areas where surface topography changes are greater. For example, at approximately 400 m along the profile, P-wave velocity equals ~1,500 ms^{-1} at a depth of ~10 m from the surface, whereas velocities exceeding 3,000 ms^{-1} are found at the same depth at approximately 200 m. A depiction of layering within the subsurface would be most apparent within the calculation of first derivative, and is evidenced by central parts of the profile displaying a rapid change in velocity gradient within the upper 2 m of the subsurface. However, this occurs at a shallower depth than the calculated wavefront inversion, and is not apparent between 120 and 180 m and from a distance of 380 m onwards, through the topographically flat northwestern end of the profile. Following forward raytracing using a finite difference algorithm, traveltimes derived from the tomographic model provided an RMS error of 1.35 ms in comparison to observed data, corresponding with 2 ms guidelines suggested for RMS where refractions are less than 30 m in depth (Sandmeier, 2020).

3.3. Electrical Resistivity Tomography

Tomograms obtained from the inversion of electrical resistivity measurements on the long profiles (Figure 5) depict a high range of inverted resistivities, with large zones of comparatively low inverted resistivities (10–100 Ωm) intercepted by near-surface areas of elevated inverted resistivity values. On Line R1, these elevated zones of increased resistivities are most apparent between 50 and 70 m, and between 170 and 220 m on the eastern side of the pingo icing (235 m). This zone is additionally shown on R2, whereby flat sections otherwise depict inverted resistivities of the order of 10–100 Ωm. Whilst the pingo icing is not within the sensitivity threshold for Line R1, Line R2 indicates inverted resistivity values the order of 100 MΩm. Where sensitive, the average R2 value for the crossover between these two profiles equaled 0.82 (see the Supporting Information S1), with weaker R2 values around the margins of inversion sensitivity.

The accumulated sensitivity matrix shown in Figure 5 indicates a complex pattern of resistivity across the pingo, as a consequence of poor contact resistance upon initial gathering of these measurements, and given the high data exclusion rate following filtering. In particular, sensitivity around the pingo icing is problematic, with dark zones of low sensitivity present at ~2–3 m depth within this structure evident for both profiles.

Shorter tomograms and associated sensitivity profiles (Figure 6) depict similar patterns in inverted resistivity and sensitivity, with low overall inverted resistivities intercepted by isolated zones of elevated inverted resistivity values which correspond well to local topographic highs. Line R3 depicts a transect across the pingo icing, whereby the topographic high provides the highest inverted resistivities (10 MΩ.m). This is flanked by zones of lower inverted resistivities within the sensitivity threshold, between 10 and 100 Ωm on the northern

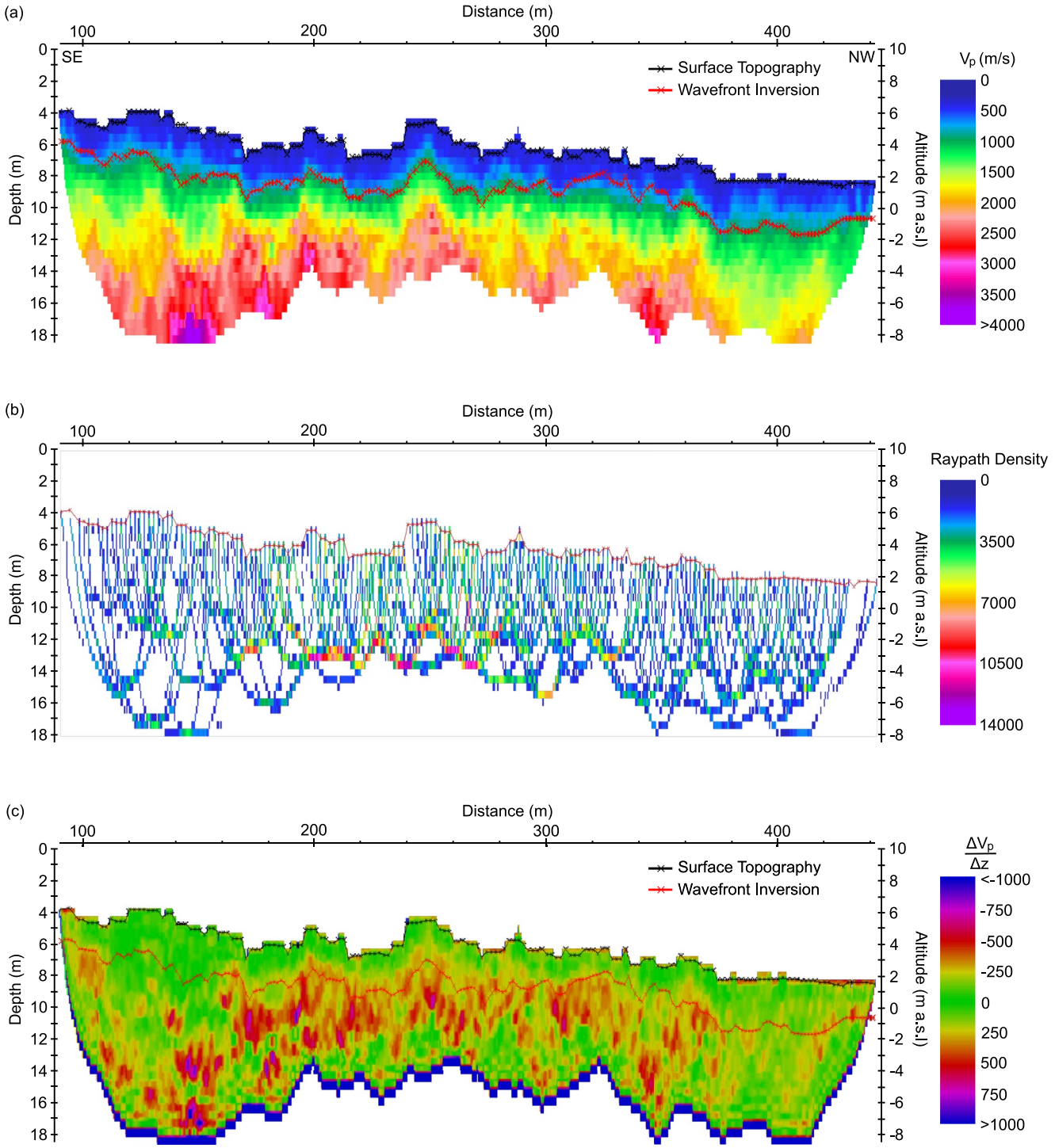

Figure 4. (a) Seismic wavefront inversion, as shown by the black line, and refraction tomography across the long line (from SE to NW) at the Lagoon Pingo site. (b) Map highlighting the density of raypaths from which the tomography was calculated. (c) The calculated and smoothed first derivative of the tomography, with the wavefront inversion overlain.

side and up to 1,000 Ωm on the southern side. Unlike longer profiles, the inversion here remains sensitive over the pingo icing, although this sensitivity is limited to the upper 5 m of the center of this profile. Line R4 shows higher inverted resistivity values (22 kΩ.m) at a depth of 5 m in the center of this profile (50 m), which occurs approximately 10 m south of the local topographic high. Line R5 also depicts a pattern of elevated inverted

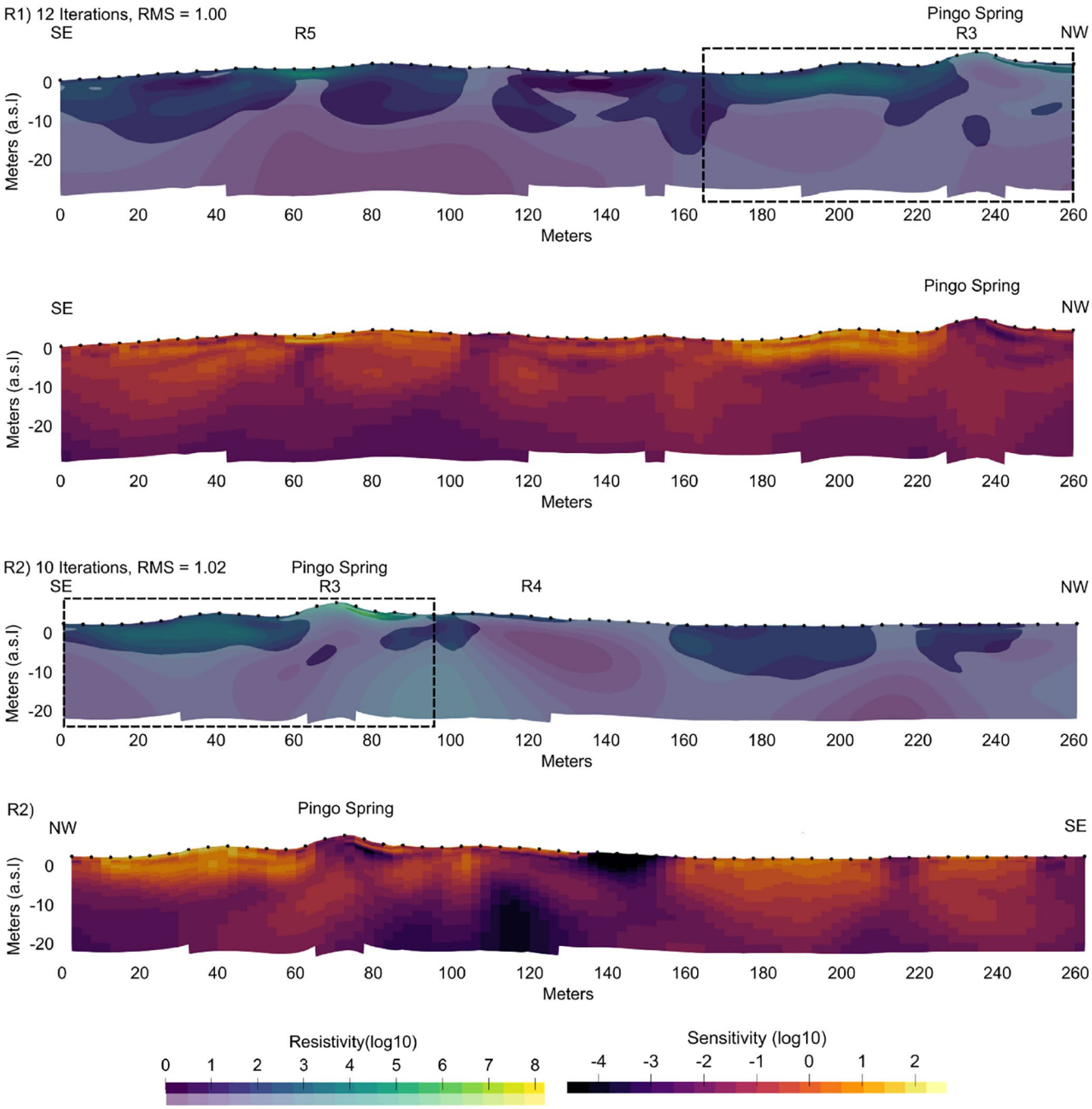

Figure 5. The final inversion results for long profiles R1 and R2, with resistivity results outside of the sensitivity threshold shown translucently, accumulated sensitivity maps shown below respective resistivity profiles, and dotted boxes showing the crossover between profiles.

resistivity values corresponding to higher elevations, with an area at approximately 70 m along the profile and at 5–15 m depth which shows an inverted resistivity of 150–300 Ωm. This contrasts with a geometric mean apparent resistivity across the profile of 44.3 Ωm. For both lines R4 and R5, high sensitivities encourage confidence in these inversions. Whilst the crossover of longer profiles and lines R3 and R4 was rendered redundant due to low sensitivities at their intersection, the crossover between R1 and R5 provided R^2 values of 0.9432 (see Supporting Information S1), which highlights that these profiles follow the same vertical trend of resistivity change.

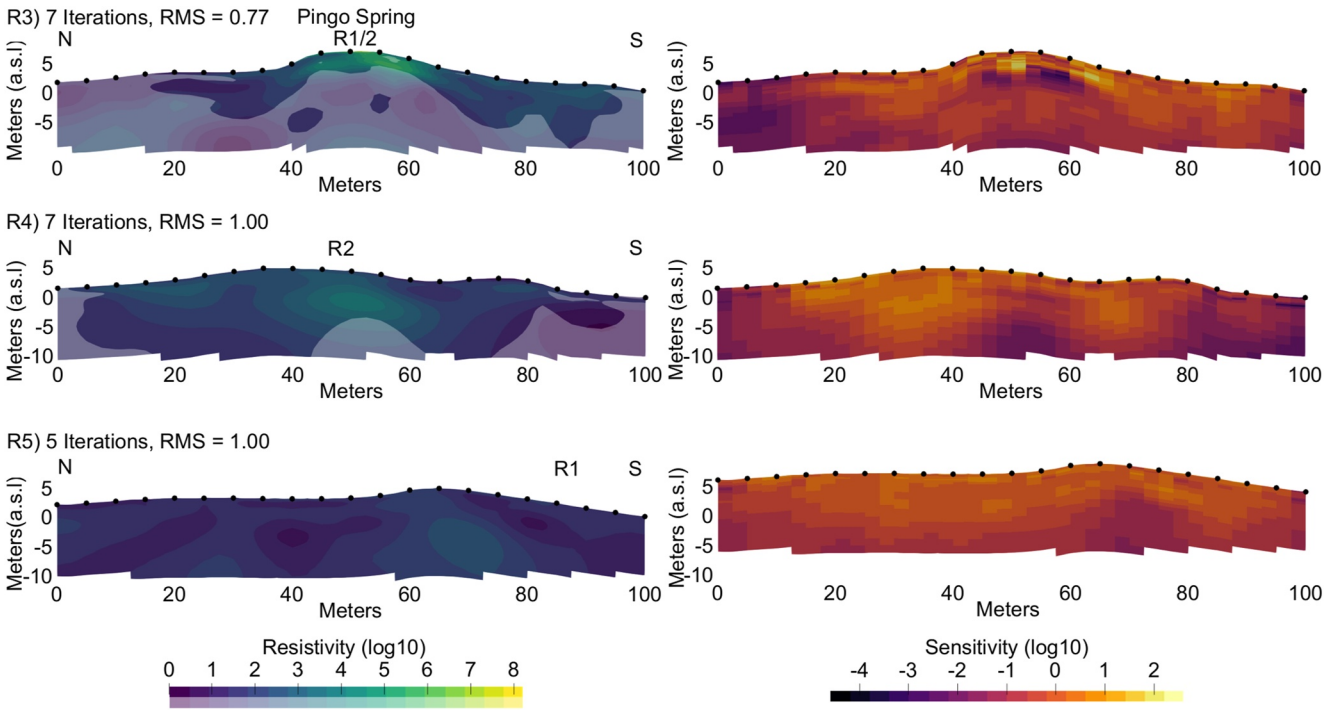

Figure 6. The final inversion and their associated accumulated sensitivity map for each of the shorter profiles.

4. Interpretation

In conducting multi-method geophysical investigations of Lagoon Pingo, we aimed to establish its composition and internal structures and to improve understanding of the mechanisms that characterize the early stages of pingo development. In particular, we test the idea that Lagoon Pingo has developed from the emergence of a submarine pockmark through active glacio-isostatic uplift of the area (Hodson et al., 2020). Our results yield insights into incipient pingo structure that does not conform with typical pingo development, and which has implications for the understanding of methane release from such landforms.

The upper layer identified from our seismic refraction data is interpreted as the active layer that covers the length and breadth of the field site. Average P-wave velocities of ~380–400 ms^{-1} correspond well with other seismic velocity measurements made in unfrozen Arctic Quaternary sediments (Hunter, 1973; Yoshikawa et al., 2006). However, this active layer is variable throughout the site, as is evidenced by wavefront inversion calculations depicting a range from 1.1 m to values exceeding 3 m. At the top end of this range, measurements are substantially thicker than active layers recorded elsewhere within Adventdalen, including 1.54 m measured at Janssonhaugen (Isaksen et al., 2001). Both geographical and measuremental factors should therefore be considered to explain this relatively thick local active layer. In terms of geographical factors, Lagoon Pingo is located at sea-level near the present coastline, and thus warmer microclimatic conditions could drive more extensive summer thaw compared to further up-valley. For example, the annual mean air temperature at the coast between 2014 and 2,018 was −1.6°C (Svalbard Lufthavn; Norwegian Meteorological Institute, 2021), compared to −3.8°C and −3.0°C for Janssonhaugen in 2017 and 2018 respectively (Christiansen et al., 2020). Additionally, saline porewater may play a role in depressing the freezing point of the local marine sediments compared to sites such as Janssonhaugen, which lies outside of the limit of marine transgression. Furthermore, given that the topographically elevated areas of the pingo have an open exposure to wind, thermally insulating snow is often scoured from these areas, thus leading to earlier exposure to solar insolation at the start of spring thaw compared to other sites. However, whilst these geographical factors may impact local active layer depths, limitations in the number of data points and in the wavelength of seismic waves (~3.9 m) may impact the wavefront inversion. Whilst the first derivative of the seismic tomography does appear to depict changes in P-wave velocity gradient within central parts of the profile, this layering is unclear within topographically flat parts of the line where calculations of active layer based on the wavefront inversion provided the greatest thicknesses. Consequently, whilst active layer thicknesses identified

elsewhere within Adventdalen (e.g., Christiansen et al., 2020; Isaksen et al., 2001) are within the error bounds of our own measurements, it is possible that these might be somewhat greater or more spatially variable at Lagoon Pingo.

In the seismic reflection data, there is an unexpected absence of clear reflections in the upper 50 m, which is inconsistent with earlier findings of Yoshikawa and Harada (1995), whose resistivity data reveal permafrost thicknesses of ~23 m. As the presence of the pingo is diagnostic of permafrost, a permafrost base should be evident. Yet, whilst frozen media ordinarily results in a substantial increase in P-wave velocity (Hauck et al., 2007), the lack of a reflection could point to a number of possible scenarios. For example, the acoustic impedance of saline permafrost and unfrozen marine sediments may be too similar to differentiate. Additionally, there could be substantial heterogeneity in permafrost thickness across Lagoon Pingo, which causes a lack of a clear reflection when combining traces by their offset between source and receiver, irrespective of their location at the site. Furthermore, a high unfrozen pore-water content within the permafrost would also serve to lower the acoustic impedance between permafrost and non-permafrost layers, which would be consistent with the valley-scale studies of Keating et al. (2018) who suggest substantial unfrozen water contents of up to ~10% in the lower parts of the valley. Indeed, previous ERT work elsewhere in Svalbard by Kasprzak et al. (2017) indicates that a bottom active layer may be present in coastal permafrost, which may provide a gradient of acoustic impedance at the permafrost base, as opposed to a clear boundary. Ultimately, the absence of a clear interface highlighting a contrast between frozen and unfrozen sediments provides uncertainty over the extent and condition of this permafrost.

At greater depths, the primary reflection visible on the common midpoint gather at 68 m is interpreted as the boundary between marine sediments and underlying shales, through both corroboration with previous research within the valley (e.g., Bælum et al., 2012) and through velocity calculations after accounting for the active layer. This is problematic for the proposed origin of Lagoon Pingo as an uplifted submarine pockmark, as it requires the fluid and gas upwelling to have persisted while high volumes of a non-hydraulically conductive substrate, that is, marine clays, were being deposited on top of it. This would require exceptional hydraulic pressures to maintain, or, alternatively, faulting or another heterogeneity to provide a viable fluid flow pathway. Whilst geological structures have been proposed as fluid flow pathways for Hytte Pingo (Hornum et al., 2021), such features are not known to occur at Lagoon Pingo and have not been identified through these geophysical investigations. While, we were unable to identify such deposits from our seismic or ERT profiles at greater depths, there is a possibility that coarse materials from a neighboring alluvial fan extend beneath the pingo from the north, which might provide at least part of the explanation.

In contrast to the seismic investigations, ERT profiles were collected during the spring when the active layer was still frozen. Although a difference in the physical properties may occur given the annual refreezing of the active layer and associated transitional zone, inverted bulk resistivities in the upper 2 m of ERT profiles (Figures 5 and 6) do not provide any indication of differences in physical properties (e.g., ice content). Instead, our survey results correspond well to visual observations made in the field at the time of the measurements. Areas of high resistivities (>10 kΩm) match areas of surface icing, including the highest resistivities occurring where the perennial central pingo spring is situated. Lower resistivities (<100 Ωm) coincide with exposed frozen marine sediments.

Elsewhere within the ERT profiles (Figures 5 and 6), and particularly at depths greater than 8 m, persistent low resistivity values (10^1–10^3 Ωm) can be interpreted as permafrost. Whilst the resistivity of permafrost is commonly between 1 and 1 MΩm (Kneisel & Hauck, 2008), previous studies conducted further up-valley (Harada & Yoshikawa, 1996; Ross et al., 2007) and in other coastal environments (Rangel et al., 2021; Yoshikawa et al., 2006) have demonstrated that permafrost resistivities can be substantially reduced in cases where sediments contain unfrozen porewater due to high dissolved salt content. Indeed, porewater salinities of 30–40 ppt have been recorded in Adventdalen (Gilbert et al., 2019). Experiments by Harada and Yoshikawa (1996) using Adventdalen sediments identify porewater salinity as a fundamental factor in the persistence of low resistivities (<100 Ωm), despite low temperatures (−8˚c) and volumetric water contents (12%). Seismic velocities support this interpretation of saline permafrost, fitting well to both previous seismic investigations in analogous environments (King et al., 1988) and effective-medium models derived from laboratory investigations (Dou et al., 2016, 2017). In the modeling of P-wave velocities provided by a fine-grained saline permafrost core, Dou et al. (2017) found velocities between 2000 and 2,500 ms^{-1} persisted where temperatures are −2°C–−5°C, which is consistent with our average value of ~2,110 ms^{-1} as revealed by the initial seismic refraction analysis, and with local climatic conditions (Christiansen et al., 2020).

Lateral variations in inverted resistivities correspond well with surface topography, with increased resistivities at depths in close proximity to, but not directly beneath local topographical highs. This trend is particularly apparent in the shorter transects obtained over the pingo, with lines R4 and R5 highlighting zones with inverted resistivities of 0.2–2.2 kΩm beneath topographically elevated parts of the profiles. Given the position of Lagoon Pingo within a glacially scoured, relatively flat valley, and with no apparent geological differences to explain an inhomogeneity, the differences in observed physical properties are expected to provide a geomorphological explanation for current pingo form and genesis. Classic pingo formation theory (e.g., Müller, 1959) dictates that a massive ground ice core is responsible for pingo uplift, formed from the near-surface freezing of pressurized groundwater. However, observed inverted resistivities of ∼2 kΩm in topographically raised areas are low compared to those commonly recorded for bodies of massive ice (generally >20 kΩm; cf. Kulessa, 2007; Vieira et al., 2008), and in comparison to icings on the surface, which despite exposure, might otherwise feature similar resistivities. One alternative explanation for the internal structure and surface geomorphology of the open-system pingo is segregation ice, whereby groundwater migrates and freezes into discrete layers within fine-grained soils, leading to pingo heave. Indeed, early notes on Adventdalen pingo morphology by Yoshikawa (1993) report on segregation ice within the immediate near-surface of the pingo, above a plano-convex massive ice core. Similar observations were reported in previous geophysical studies at Longyear and Hytte pingos (Ross et al., 2007), whereby resistivities of <2 kΩm in topographical highs were interpreted as segregation ice, although no massive ice core was identified. Furthermore, geophysical investigations of an open-system pingo in Yukon, Canada also failed to observe a massive ice core, proposing segregation ice as the primary frozen component (Kunz & Kneisel, 2021). Notably, their ERT profiles also depicted higher inverted resistivities in close proximity, yet not directly beneath, local topographic highs, which was interpreted as the most significant ground ice occurring towards the flanks of the pingos. Our observations echo these studies, which gives confidence in our interpretation that the observed low resistivities and a relatively low topographic imprint is segregation ice serving as the primary geomorphic component.

Replicable negative resistivities obtained in the long profiles are also consistent with the presence of segregation ice lenses. These occurred in areas of higher elevation (e.g., R1 170–220 m; see Figure 5) that are not presently influenced by the upwelling groundwater spring. Whilst negative resistivities have often been regarded as erroneous (Jung et al., 2009), we argue that the occurrence of negative apparent resistivity on both normal and reciprocal profiles (see Supporting Information S1) meets our stringent data filtering criteria and do not constitute data quality issues. As recent numerical and modeling studies have shown, negative resistivities may arise in specific field scenarios. For example, through a series of dipole-dipole array numerical simulations, Jung et al. (2009) demonstrated the occurrence of negative resistivity values as a consequence of U- or crescent-shaped geological structures. In addition, Lee and Cho (2020) indicate that an extreme range of resistivities may also result in negative apparent resistivities. Elements of both of these factors may hold true at Lagoon Pingo. For example, the dome-shaped winter and spring icing occurs in a depression that is occupied in the summer by a small pond. This shape resembles the crescent-shaped geological structure described in the former scenario. In respect to the latter scenario, an extreme range of resistivities (10^8 Ωm) at the Lagoon Pingo site is caused by the close proximity of extensive yet highly resistive surface icings, segregation ice within the near surface and otherwise electrically conductive clays. This extreme range (10^8 Ωm) may additionally provide an explanation for negative apparent resistivities despite using a Wenner configuration, which is more robust and less susceptible to noise when compared to the aforementioned studies whereby dipole-dipole configurations were used. Yet whilst results here correspond well to previous modeling studies, further ground truthing is required to confirm the validity of the interpretation of these negative resistivities, and their occurrence in permafrost environments.

5. Discussion

5.1. Pingo Genesis

Previous studies have suggested that Lagoon Pingo provides an example of a glacio-isostatically uplifted pockmark, formed following the emergence of a pre-existing methane seep. This presumes that the flow pathway existed prior to terrestrial exposure. Yet whilst the recent development (140 ± 20 years BP) of the terrestrial pingo is evidenced through radiocarbon dates of mollusc shells (Yoshikawa & Nakamura, 1996), the presence of a seismic interface at ∼68 m depth, interpreted as the boundary between Holocene marine sediments and underlying shale bedrock is problematic for this formation process. Given that these fine-grained marine sediments have

low hydraulic conductivity (Olaussen et al., 2020), it is difficult to perceive how the groundwater upwelling was under sufficient hydraulic pressure to persist through the accumulation of these sediments above it.

Despite detailed and targeted surveys, it remains unknown whether a heterogeneity exists that would enable the preferential flow of groundwater through the non-hydraulically conductive sediments at Lagoon Pingo, and whether such heterogeneities influence other coastal methane seeps and pockmarks. For example, whilst recent geophysical investigations have determined that Hytte Pingo is formed above an important geological boundary (Hornum et al., 2021), no known geological interfaces or faults (cf. Ciric, 2019) underlie Lagoon Pingo, nor have such features been identified within this geophysical study. Despite this, the presence of a groundwater spring necessitates a fluid flow pathway (Yoshikawa & Harada, 1995). One potential explanation for enhanced groundwater flow in the subsurface is that coarse-grained sediments, such as sand and gravel from the alluvial fan located to the north of the pingo, may extend beneath the pingo, providing a hydraulically conductive heterogeneity which enables groundwater flow. This has previously been discussed by Humlum et al. (2003), who suggest that unfrozen groundwater may flow within the lowermost layers of coarse-grained deposits above impermeable permafrost, before pressurization where these deposits thin at the alluvial fan base. Whilst this scenario does not explain the observed emission of methane per se (Hodson et al., 2019, 2020), or would necessarily be compatible with the local thickness of permafrost derived by Yoshikawa and Harada (1995), the alluvial fan could provide sufficient coarse-grained sediment to enable a glacio-isostatically uplifted pockmark system to persist terrestrially.

5.2. Structural Controls and Pingo Formational Processes

In contrast to uncertainties regarding the deeper geological structures at Lagoon Pingo, the geophysical data presented here provide insight into the near-surface structure of incipient pingos and the nature of their formation within predominantly fine-grained sediments. In this study, segregation ice provides the most plausible explanation for the topography of the pingo, provided the overall context of the field site, and the characteristics identified within the geophysical data. Whilst previous studies have identified segregation ice within open-system pingo forms (Ross et al., 2007; Yoshikawa, 1993), it has largely been associated with late stages of pingo growth and development (Mackay, 1973, 1985). Our interpretation of segregation ice within the incipient Lagoon Pingo, and the conspicuous absence of a massive ice core calls for a reconsideration of early open-system pingo formational processes.

In explaining the present-day geomorphology and architecture of Lagoon Pingo, we suggest two primary controls on incipient pingo development: sedimentology and groundwater availability. In regard to sedimentology, fine-grained soils facilitate the formation of segregation ice (Smith, 1985), whereby thin lenses of ice form as water is drawn (via cryosuction) to the freezing plane. As fine-grained sediments feature smaller pores, capillary action tends to be greater, and thus a greater negative pressure is exerted upon liquid water. Coarser-grained, more permeable sediments in contrast are better suited for ground ice formation (Pissart, 2002), perhaps explaining the absence of injection ice emblematic of traditional pingo structures (Ballantyne, 2018).

In terms of groundwater availability, the in-flow of upwelling groundwater provides a localised region of elevated moisture contents that is conducive to enhanced segregation ice formation. At Lagoon Pingo, this may be further aided by differences in the groundwater chemistry between the pingo spring and porewater within the sediment. Existing electrical conductivity measurements on the groundwater spring provide relatively low values of 5–8 mS cm^{-1} (Hodson et al., 2019; Hornum et al., 2020), when compared with typical values of ~17 mS cm^{-1} (Cable et al., 2018) for porewaters elsewhere in Adventdalen. Whilst the exact nature of the intrusion of upwelling groundwater through marine sediments and permafrost is unknown, groundwaters with lower solute content would be more susceptible to freezing, and would offer part of the explanation for why segregation ice formation could be more prominent here compared to elsewhere within the valley. The low hydraulic conductivity of the marine sediments within Lagoon Pingo would also contribute by limiting the lateral migration of these upwelling groundwaters, resulting in a locally high moisture contents and lower groundwater resistivity that enhances freezing activity.

Parallels can be drawn between the current geomorphology of Lagoon Pingo and lithalsas in fine-grained alluvial or lacustrine environments (Wolfe et al., 2014). In both cases, segregation ice plays a prominent role as a result of elevated moisture availability and sediments with poor permeability, thus promoting cryosuction processes. Whilst

many contemporary lithalsas occur in close association with surface water bodies that provide the moisture required for cryosuction and frost heave (Wolfe et al., 2014), the existing groundwater upwelling at Lagoon Pingo provides this moisture, enabling increased segregation ice formation relative to the surrounding area in which saline porewater dominates. Additionally, the fine-grained nature of marine clays within Adventdalen bear similarities to sediments within structurally similar lithalsas, including on Holocene plateaus in Northern Quebec (Allard et al., 1996). We therefore propose that Lagoon Pingo, in its present form, represents a hybrid form, with a lithalsa-esque internal structure punctuated by the hydraulically pressurised spring typical of traditional open-system pingos.

If there is a genetic relationship between incipient Lagoon Pingo and other pingo forms further up-valley (Longyear and Hytte Pingo), it remains unclear how our interpretation of segregation ice in early stage pingo development may evolve into more established open-system pingo forms. Whilst Ross et al. (2007) provide a similar interpretation of low resistivities (<2 kΩm) as suggesting segregation ice within Longyear and Hytte pingos, it is difficult to conceive how segregation ice could be responsible for ∼20 m of elevation heave. Recent drilling elsewhere on Svalbard also casts doubt on segregation ice providing the dominant structure within established open-system pingos. In the coring of marine-based pingos in Grøndalen, Demidov et al. (2019) demonstrate massive ice exceeding 20 m in thickness beneath a pingo of 9 m height. Whilst numerical simulations of palsas and lithalsas analogous to our proposed structure of Lagoon Pingo have demonstrated that segregation ice can produce ∼6 m of heave over a period of 150 years (An & Allard, 1995), further coring is necessary to validate the precise architecture of frozen ground within these pingos.

5.3. Implications on Spring Emergence and Methane Emission Mechanism

Our interpretation of a segregation ice dominated incipient pingo form may have wider significance on the emission mechanisms of deeply seated methane within continuous permafrost environments. Whereas, injection ice would ordinarily preclude cryopegs or conduits through which fluid flow can occur, segregation ice can persist as discrete ice lenses between unfrozen sediment pockets. Additionally, elevated ice contents and segregated ice lenses within the sediment are likely to influence local pore pressures, and may interact with or otherwise maintain the groundwater spring. However, without discerning the nature of the groundwater upwelling (e.g., whether water in-flow occurs under a diffusive or advective conduit-like regime), it is difficult to establish the exact nature of the influence of such structures. Further research, particularly coring, would be required to provide the necessary insight into the exact nature of pressurized groundwater flow within permafrost.

6. Conclusions

Using a combination of active seismic and ERT data, this study interprets the internal structure and characteristics of an incipient open-system pingo. The pingo releases a substantial methane flux to the atmosphere, and its terrestrial genesis was previously attributed to the uplift of a submarine pockmark (Hodson et al., 2019, 2020). Our findings call for an alternative hypothesis given the thick layer of Holocene marine deposits (∼68 m) which would have been deposited on the active submarine spring, though this cannot be entirely discounted due to the possible role of local coarse alluvial fan sediments in changing hydraulic conductivities of sub-pingo materials.

Our speculation that segregation ice is dominant within an incipient pingo form is at odds with established theories of open-system pingo formation, which presume that initial growth normally occurs through the formation of injection ice following the near-surface freezing of pressurized groundwater. This study highlights sediment grain size as a fundamental control on early pingo formation, with fine-grained sediments such as those in Holocene marine environments providing high porewater pressures conducive to segregation ice formation. Moisture content provides an additional control, and is sourced by the groundwater spring which further facilitates localized pingo formation. We therefore speculate that the result is a landform with an internal structure analogous to a lithalsa, yet with the mechanism of a typical open-system pingo. However, in absence of definitive evidence of segregation ice beneath Lagoon Pingo, future work, which may include coring and time-lapse resistivity imaging, is required to fully elucidate the subsurface nature of this incipient landform.

Our study highlights the continued uncertainty over pingo genesis and development. Whilst segregation ice has previously been proposed as playing an important role in pingo growth, its presence within an incipient form is ambiguous and indicates further plurality in the genesis of pingo landforms. This structure likely influences local

porosities and pressure regimes, and may therefore impact upon groundwater upwelling and subsequent methane release. Despite this, as our geophysical data did not discern the the actual flowpath of groundwater through the sub-zero sediments, there remains a need for further study of subpermafrost and intrapermafrost groundwater migration.

Data Availability Statement

The data supporting the conclusions of this paper are publicly available from Zenodo (https://doi.org/10.5281/zenodo.4593831).

Acknowledgments
Fieldwork was financially supported by the Swansea University College of Science Research Fund 2018/19, the Near Surface Geophysics Group of the Geological Society of London's Postgraduate Fieldwork Fund, and by the Research Council of Norway through its Centre of Excellence funding scheme (Grant No. 223259). Fieldwork was conducted within the CLIMAGAS project, funded by the Research Council of Norway (project no: 294764). Sara Mollie Cohen and UNIS logistics are thanked for the loan of ERT instruments, and for fieldwork logistical support. Richard Hann and Armin Dachauer are thanked for providing the Structure-from-Motion DEM (Hann & Dachauer, 2020). Emma Ciric, James Davidson, Veerle van Winden, Viktor Kröger, Will Hartz, Mikkel Toft Hornum, and Naomi Ochwat are thanked for fieldwork assistance. CPH is funded by a postgraduate scholarship awarded by the College of Science, Swansea University and by the Research Council of Norway through its Centre of Excellence funding scheme (Grant No. 223259). The authors also thank editors Cathleen Jones and Amy East, and Andrew Parsekian, Mariusz Majdański and one anonymous reviewer for their constructive comments on an earlier version of this manuscript.

References

Allard, M., Caron, S., & Bégin, Y. (1996). Climatic and ecological controls on ice segregation and thermokarst: The case history of a permafrost plateau in Northern Quebec. *Permafrost and Periglacial Processes*, *7*(3), 207–227. https://doi.org/10.1002/(sici)1099-1530(199609)7:3<207::aid-ppp219>3.0.co;2-4

An, W., & Allard, M. (1995). A mathematical approach to modelling palsa formation: Insights on processes and growth conditions. *Cold Regions Science and Technology*, *23*, 231–244. https://doi.org/10.1016/0165-232X(94)00015-P

Andreassen, K., Hubbard, A., Winsborrow, M., Patton, H., Vadakkepuliyambatta, S., Plaza-Faverola, A., et al. (2017). Massive blow-out craters formed by hydrate-controlled methane expulsion from the Arctic seafloor. *Science*, *356*(6341), 948–953. https://doi.org/10.1126/science.aal4500

Auriac, A., Whitehouse, P. L., Bentley, M. J., Patton, H., Lloyd, J. M., & Hubbard, A. (2016). Glacial isostatic adjustment associated with the Barents Sea ice sheet: A modelling inter-comparison. *Quaternary Science Reviews*, *147*, 122–135. https://doi.org/10.1016/j.quascirev.2016.02.011

Ballantyne, C. K. (2018). *Periglacial geomorphology*. Wiley-Blackwell.

Bælum, K., Johansen, T. A., Johnsen, H., Rød, K., Ruud, B. O., & Braathen, A. (2012). Subsurface structures of the Longyearbyen CO_2 Lab study area in Central Spitsbergen (Arctic Norway), as mapped by reflection seismic data. *Norwegian Journal of Geology*, *92*, 377–389.

Binley, A., & Kemna, A. (2005). DC resistivity and induced polarization methods. In Y. Rubin & S. S. Hubbard (Eds.), *Hydrogeophysics* (pp. 129–156). Springer.

Binley, A., Ramirez, A., & Daily, W. (1995). Regularised image reconstruction of noisy electrical resistance tomography data. In M. S. Beck, B. S. Hoyle, M. A. Morris, R. C. Waterfall, & R. A. Williams (Eds.), *Process tomography – 1995, Proceedings of the 4th workshop of the European concerted action on process tomography* (pp. 6401–8410).

Blanchy, G., Saneiyan, S., Boyd, J., McLachlan, P., & Binley, A. (2020). ResIPy, an intuitive open source software for complex geoelectrical inversion/modeling. *Computers & Geosciences*, *137*, 104423. https://doi.org/10.1016/j.cageo.2020.104423

Bradford, J. H. (2002). Depth characterization of shallow aquifers with seismic reflection, Part I—the failure of NMO velocity analysis and quantitative error prediction. *Geophysics*, *67*(1), 89–97. https://doi.org/10.1190/1.1451362

Bradford, J. H., & Sawyer, D. S. (2002). Depth characterization of shallow aquifers with seismic reflection, Part II—Prestack depth migration and field examples. *Geophysics*, *67*(1), 98–109. https://doi.org/10.1190/1.1451372

Cable, S., Elberling, B., & Kroon, A. (2018). Holocene permafrost history and cryostratigraphy in the High-Arctic Adventdalen Valley, central Svalbard. *Boreas*, *47*(2), 423–442. https://doi.org/10.1111/bor.12286

Christiansen, H. H., Etzelmüller, B., Isaksen, K., Juliussen, H., Farbrot, H., Humlum, O., et al. (2010). The thermal state of permafrost in the Nordic area during the International Polar Year 2007–2009. *Permafrost and Periglacial Processes*, *21*(2), 156–181. https://doi.org/10.1002/ppp.687

Christiansen, H. H., Gilbert, G. L., Demidov, N., Guglielmin, M., Isaksen, K., Osuch, M., & Boike, J. (2020). Permafrost temperatures and active layer thickness in Svalbard during 2017/2018 (PermaSval). (pp. 236–249). In F. Van den Heuvel, C. Hübner, M. Błaszczyk, M. Heimann, & H. Lihavainen (Eds.), *SESS report 2019. Longyearbyen, Svalbard: Svalbard Integrated Arctic Earth observing system.*

Ciric, E. N. (2019). *Methane escape from lowland terrestrial seepages: Links to deglaciation and permafrost dynamics (MSc Thesis)*. Universidade Do Algarve. Retrieved from https://sapientia.ualg.pt/bitstream/10400.1/13728/1/Dissertac_ao%2BEmma%2BCiric.pdf

Demidov, N., Wetterich, S., Verkulich, S., Ekaykin, A., Meyer, H., Anisimov, M., et al. (2019). Pingo development in Grøndalen, West Spitsbergen. *The Cryosphere*, *13*, 3155–3169. https://doi.org/10.5194/tc-13-3155-2019

Dix, C. H. (1955). Seismic velocities from surface measurements. *Geophysics*, *20*, 180–195. https://doi.org/10.1190/1.1438126

Dou, S., Nakagawa, S., Dreger, D., & Ajo-Franklin, J. (2016). A rock-physics investigation of unconsolidated saline permafrost: P-wave properties from laboratory ultrasonic measurements. *Geophysics*, *81*(1), WA233–WA245. https://doi.org/10.1190/geo2015-0176.1

Dou, S., Nakagawa, S., Dreger, D., & Ajo-Franklin, J. (2017). An effective-medium model for P-wave velocities of saturated, unconsolidated saline permafrost. *Geophysics*, *82*(3), EN33–EN50. https://doi.org/10.1190/geo2016-0474.1

French, H. M. (2007). *The periglacial environment* (4th ed.). John Wiley & Sons. https://doi.org/10.1002/978111913e2820

Gilbert, G. L., Instanes, A., Sinitsyn, A. O., Aalberg, A., & Aalberg, A. (2019). Characterization of two sites for geotechnical testing in permafrost: Longyearbyen, Svalbard. *AIMS Geosciences*, *5*(4), 868–885. https://doi.org/10.3934/geosci.2019.4.868

Gilbert, G. L., O'Neill, H. B., Nemec, W., Thiel, C., Christiansen, H. H., & Buylaert, J.-P. (2018). Late Quaternary sedimentation and permafrost development in a Svalbard fjord-valley, Norwegian high Arctic. *Sedimentology*, *65*(7), 2531–2558. https://doi.org/10.1111/sed.12476

Grünberg, I., Wilcox, E. J., Zwieback, S., Marsh, P., & Boike, J. (2020). Linking tundra vegetation, snow, soil temperature, and permafrost. *Biogeosciences*, *17*(16), 4261–4279. https://doi.org/10.5194/bg-17-4261-2020

Gurney, S. D. (1998). Aspects of the genesis and geomorphology of pingos: Perennial permafrost mounds. *Progress in Physical Geography*, *22*(3), 307–324. https://doi.org/10.1177/030913339802200301

Hann, R., & Dachauer, A. (2020). *Drone-based mapping of the lagoon pingo in Svalbard* (Version 1) [Data set]. DataverseNO. https://doi.org/10.18710/IMPEG8

Harada, K., & Yoshikawa, K. (1996). Permafrost age and thickness near Adventfjorden, Spitsbergen. *Polar Geography*, *20*(4), 267–281. https://doi.org/10.1080/10889379609377607

Harris, S. A., Brouchkov, A., & Guodong, C. (2017). *Geocryology: Characteristics and use of frozen ground and permafrost landforms* (1st ed.). CRC Press. https://doi.org/10.4324/9781315166988

Hauck, C., Vieira, G., Gruber, S., Blanco, J., & Ramos, M. (2007). Geophysical identification of permafrost in Livingston Island, maritime Antarctica. *Journal of Geophysical Research*, *112*(F2), F02S19. https://doi.org/10.1029/2006jf000544

Hauck, C., & Vonder Mühll, D. (2003). Inversion and interpretation of two-dimensional geoelectrical measurements for detecting permafrost in mountainous regions. *Permafrost and Periglacial Processes*, *14*(4), 305–318. https://doi.org/10.1002/ppp.462

Hodson, A. J., Nowak, A., Hornum, M. T., Senger, K., Redeker, K., Christiansen, H. H., et al. (2020). Sub-permafrost methane seepage from open-system pingos in Svalbard. *The Cryosphere*, *14*(11), 3829–3842. https://doi.org/10.5194/tc-14-3829-2020

Hodson, A. J., Nowak, A., Redeker, K. R., Holmlund, E. S., Christiansen, H. H., & Turchyn, A. V. (2019). Seasonal dynamics of methane and carbon dioxide from an open system pingo: Lagoon Pingo, Svalbard. *Frontiers of Earth Science*, *7*, 30. https://doi.org/10.3389/feart.2019.00030

Hornum, M. T., Betlem, P., & Hodson, A. (2021). Groundwater flow through continuous permafrost along geological boundary revealed by electrical resistivity tomography. *Geophysical Research Letters*, *48*(14), e2021GL092757. https://doi.org/10.1029/2021GL092757

Hornum, M. T., Hodson, A. J., Jessen, S., Bense, V., & Senger, K. (2020). Numerical modelling of permafrost spring discharge and open-system pingo formation induced by basal permafrost aggradation. *The Cryosphere*, *14*(12), 4627–4651. https://doi.org/10.5194/tc-14-4627-2020

Humlum, O. (2005). Holocene permafrost aggradation in Svalbard. *Geological Society London Special Publications*, *242*(1), 119–129. https://doi.org/10.1144/GSL.SP.2005.242.01.11

Humlum, O., Instanes, A., & Sollid, J. L. (2003). Permafrost in Svalbard: A review of research history, climatic background and engineering challenges. *Polar Research*, *22*(2), 191–215. https://doi.org/10.1111/j.1751-8369.2003.tb00107.x

Hunter, J. A. M. (1973). The application of shallow seismic methods to mapping of frozen surcial materials. In *Proceedings of the second international conference on permafrost* (pp. 527–535). National Academy of Sciences.

Isaksen, K., Holmlund, P., Sollid, J. L., & Harris, C. (2001). Three deep alpine-permafrost boreholes in Svalbard and Scandinavia. *Permafrost and Periglacial Processes*, *12*(1), 13–25. https://doi.org/10.1002/ppp.380

Jung, H.-K., Min, D.-J., Lee, H. S., Oh, S., & Chung, H. (2009). Negative apparent resistivity in dipole–dipole electrical surveys. *Exploration Geophysics*, *40*(1), 33–40. https://doi.org/10.1071/EG08111

Kasprzak, M. (2015). High-resolution electrical resistivity tomography applied to patterned ground, Wedel Jarlsberg Land, south-west Spitsbergen. *Polar Research*, *34*, 25678. https://doi.org/10.3402/polar.v34.25678

Kasprzak, M., Strzelecki, M. C., Traczyk, A., Kondracka, M., Lim, M., & Migała, K. (2017). On the potential for a bottom active layer below coastal permafrost: The impact of seawater on permafrost degradation imaged by electrical resistivity tomography (Hornsund, SW Spitsbergen). *Geomorphology*, *293*, 347–359.

Keating, K., Binley, A., Bense, V., Dam, R. L. V., & Christiansen, H. H. (2018). Combined geophysical measurements provide evidence for unfrozen water in permafrost in the Adventdalen Valley in Svalbard. *Geophysical Research Letters*, *45*(15), 7606–7614. https://doi.org/10.1029/2017gl076508

Kemna, A. (2000). *Tomographic inversion of complex resistivity: Theory and application (PhD Thesis)*. University of BonnUniversity of Bochum. Retrieved from https://www.geo.uni-bonn.de/mitarbeiter/Andreas-Kemna/dissertation

King, M. S., Zimmerman, R. W., & Corwin, R. F. (1988). Seismic and electrical properties of unconsolidated Permafrost1. *Geophysical Prospecting*, *36*(4), 349–364. https://doi.org/10.1111/j.1365-2478.1988.tb02168.x

Klein, K. A., & Santamarina, J. C. (2003). Electrical conductivity in soils: Underlying phenomena. *Journal of Environmental & Engineering Geophysics*, *8*(4), 263–273. https://doi.org/10.4133/JEEG8.4.263

Kneisel, C., & Hauck, C. (2008). Electrical methods. In C. Hauck, & C. Kniesel (Eds.), *Applied geophysics in periglacial environments* (pp. 3–27). Cambridge University Press.

Koestel, J., Kemna, A., Javaux, M., Binley, A., & Vereecken, H. (2008). Quantitative imaging of solute transport in an unsaturated and undisturbed soil monolith with 3-D ERT and TDR. *Water Resources Research*, *44*(12), W12411. https://doi.org/10.1029/2007WR006755

Koven, C. D., Ringeval, B., Friedlingstein, P., Ciais, P., Cadule, P., Khvorostyanov, D., et al. (2011). Permafrost carbon-climate feedbacks accelerate global warming. *Proceedings of the National Academy of Sciences*, *108*(36), 14769–14774. https://doi.org/10.1073/pnas.1103910108

Kulessa, B. (2007). A critical review of the low-frequency electrical properties of ice sheets and glaciers. *Journal of Environmental & Engineering Geophysics*, *12*(1), 23–36. https://doi.org/10.2113/JEEG12.1.23

Kunz, J., & Kneisel, C. (2021). Three-dimensional investigation of an open- and a closed-system Pingo in northwestern Canada. *Permafrost and Periglacial Processes*, *32*, 1–17. https://doi.org/10.1002/ppp.2115

Lawrence, D. M., Koven, C. D., Swenson, S. C., Riley, W. J., & Slater, A. G. (2015). Permafrost thaw and resulting soil moisture changes regulate projected high-latitude CO_2 and CH_4 emissions. *Environmental Research Letters*, *10*(9), 094011. https://doi.org/10.1088/1748-9326/10/9/094011

Lawrence, D. M., Slater, A. G., Romanovsky, V. E., & Nicolsky, D. J. (2008). Sensitivity of a model projection of near-surface permafrost degradation to soil column depth and representation of soil organic matter. *Journal of Geophysical Research*, *113*(F2), F02011. https://doi.org/10.1029/2007JF000883

Lee, K. S., & Cho, I. K. (2020). Negative apparent resistivities in surface resistivity measurements. *Journal of Applied Geophysics*, *176*, 104010. https://doi.org/10.1016/j.jappgeo.2020.104010

Léger, E., Dafflon, B., Soom, F., Peterson, J., Ulrich, C., & Hubbard, S. (2017). Quantification of arctic soil and permafrost properties using ground-penetrating radar and electrical resistivity tomography datasets. *IEEE Journal of Selected Topics in Applied Earth Observations and Remote Sensing*, *10*(10), 4348–4359. https://doi.org/10.1109/JSTARS.2017.2694447

Liestøl, O. (1977). Pingos, springs and permafrost in Spitsbergen. In *Norsk Polarinstitutt Arbok* (pp. 7–29). Norwegian Polar Institute.

Lønne, I., & Nemec, W. (2004). High-arctic fan delta recording deglaciation and environment disequilibrium. *Sedimentology*, *51*(3), 553–589. https://doi.org/10.1111/j.1365-3091.2004.00636.x

Loranty, M. M., Abbott, B. W., Blok, D., Douglas, T. A., Epstein, H. E., Forbes, B. C., et al. (2018). Reviews and syntheses: Changing ecosystem influences on soil thermal regimes in northern high-latitude permafrost regions. *Biogeosciences*, *15*(17), 5287–5313. https://doi.org/10.5194/bg-15-5287-2018

Mackay, J. R. (1973). The growth of pingos, western Arctic Coast, Canada. *Canadian Journal of Earth Sciences*, *10*(6), 979–1004. https://doi.org/10.1139/e73-086

Mackay, J. R. (1985). Pingo ice of the western Arctic Coast, Canada. *Canadian Journal of Earth Sciences*, *22*(10), 1452–1464. https://doi.org/10.1139/e85-151

Major, H., Haremo, P., Dallmann, W. K., & Andresen, A. (2001). *Geological map of Svalbard 1:100 000, Sheet C9G: Adventdalen*. Norwegian Polar Institute.

Mishra, U., Hugelius, G., Shelef, E., Yang, Y., Strauss, J., Lupachev, A., et al. (2021). Spatial heterogeneity and environmental predictors of permafrost region soil organic carbon stocks. *Science Advances*, *7*(9), eaaz5236. https://doi.org/10.1126/sciadv.aaz5236

Mollaret, C., Hilbich, C., Pellet, C., Flores-Orozco, A., Delaloye, R., & Hauck, C. (2019). Mountain permafrost degradation documented through a network of permanent electrical resistivity tomography sites. *The Cryosphere*, *13*(10), 2557–2578. https://doi.org/10.5194/tc-13-2557-2019

Morelli, G., & LaBrecque, D. J. (1996). Advances in ERT inverse modeling. *European Journal of Environmental and Engineering Geophysics*, *1*, 171–186.

Müller, F. (1959). *Beobachtungen über Pingos: Detailuntersuchungen in Ostgrönland und in der kanadischen Arktis*. CA Reitzelsforlag.

Nisbet, E. G., Dlugokencky, E. J., Manning, M. R., Lowry, D., Fisher, R. E., France, J. L., et al. (2016). Rising atmospheric methane: 2007–2014 growth and isotopic shift. *Global Biogeochemical Cycles*, *30*, 1356–1370. https://doi.org/10.1002/2016GB005406

Norwegian Meterological Institute. (2021). *Norwegian centre for climate services*. Retrieved from https://seklima.met.no/

Norwegian Polar Institute (2014). Terrengmodell Svalbard (S0 Terrengmodell) [Data set]. Norwegian Polar Institute. https://doi.org/10.21334/npolar.2014.dce53a47

Olaussen, S., Senger, K., Braathen, A., Grundvåg, S.-A., & Mørk, A. (2020). You learn as long as you drill; research synthesis from the Longyearbyen CO_2 Laboratory, Svalbard, Norway. *Norwegian Journal of Geology*, *99*. https://doi.org/10.17850/njg008

Park, S. K., & Van, G. P. (1991). Inversion of pole-pole data for 3-D resistivity structure beneath arrays of electrodes. *Geophysics*, *56*(7), 951–960. https://doi.org/10.1190/1.1443128

Pirk, N., Mastepanov, M., López-Blanco, E., Christensen, L. H., Christiansen, H. H., & Hansen, B. U. (2017). Toward a statistical description of methane emissions from arctic wetlands. *Ambio*, *46*(1), 70–80. https://doi.org/10.1007/s13280-016-0893-3

Pissart, A. (2002). Palsas, lithalsas and remnants of these periglacial mounds. A progress report. *Progress in Physical Geography*, *26*(4), 605–621. https://doi.org/10.1191/0309133302pp354ra

Pithan, F., & Mauritsen, T. (2014). Arctic amplification dominated by temperature feedbacks in contemporary climate models. *Nature Geoscience*, *7*(3), 181–184. https://doi.org/10.1038/ngeo2071

Portnov, A., Smith, A. J., Mienert, J., Cherkashov, G., Rekant, P., Semenov, P., et al. (2013). Offshore permafrost decay and massive seabed methane escape in water depths >20m at the South Kara Sea shelf. *Geophysical Research Letters*, *40*(15), 3962–3967. https://doi.org/10.1002/grl.50735

Rangel, R. C., Parsekian, A. D., Farquharson, L. M., Jones, B. M., Ohara, N., Creighton, A. L., et al. (2021). Geophysical observations of Taliks below drained lake basins on the arctic coastal plain of Alaska. *Journal of Geophysical Research: Solid Earth*, *126*(3), e2020JB020889. https://doi.org/10.1029/2020JB020889

Revil, A., & Glover, P. W. J. (1998). Nature of surface electrical conductivity in natural sands, sandstones, and clays. *Geophysical Research Letters*, *25*(5), 691–694. https://doi.org/10.1029/98GL00296

Ross, N., Brabham, P. J., Harris, C., & Christiansen, H. H. (2007). Internal structure of open system pingos, adventdalen, Svalbard: The use of resistivity tomography to assess ground-ice conditions. *Journal of Environmental & Engineering Geophysics*, *12*(1), 113–126. https://doi.org/10.2113/jeeg12.1.113

Rossi, G., Accaino, F., Boaga, J., Petronio, L., Romeo, R., & Wheeler, W. (2018). Seismic survey on an open pingo system in adventdalen valley, Spitsbergen, Svalbard. *Near Surface Geophysics*, *16*(1), 1–15. https://doi.org/10.3997/1873-0604.2017037

Sandmeier, K. J. (2020). *REFLEXW version 9.5*. Retrieved online: Retrieved from https://www.sandmeier-geo.de/Download/reflexw_manual_a4.pdf

Schrott, L., & Hoffmann, T. (2008). Refraction seismics. In C. Hauck & C. Kniesel (Eds.), *Applied Geophysics in periglacial environments* (pp. 57–80). Cambridge University Press.

Schrott, L., & Sass, O. (2008). Application of field geophysics in geomorphology: Advances and limitations exemplified by case studies. *Geomorphology*, *93*(1), 55–73. https://doi.org/10.1016/j.geomorph.2006.12.024

Schwamborn, G. J., Dix, J. K., Bull, J. M., & Rachold, V. (2002). High-resolution seismic and ground penetrating radar–geophysical profiling of a thermokarst lake in the western Lena Delta, Northern Siberia. *Permafrost and Periglacial Processes*, *13*(4), 259–269. https://doi.org/10.1002/ppp.430

Serov, P., Vadakkepuliyambatta, S., Mienert, J., Patton, H., Portnov, A., Silyakova, A., et al. (2017). Postglacial response of Arctic Ocean gas hydrates to climatic amelioration. *Proceedings of the National Academy of Sciences*, *114*(24), 6215–6220. https://doi.org/10.1073/pnas.1619288114

Sjöberg, Y., Marklund, P., Pettersson, R., & Lyon, S. W. (2015). Geophysical mapping of palsa peatland permafrost. *The Cryosphere*, *9*(2), 465–478. https://doi.org/10.5194/tc-9-465-2015

Smith, M. W. (1985). Models of soil freezing. In M. Church & O. Slaymaker (Eds.), *Field and theory: Lectures in Geocryology* (pp. 96– 120). University of British Columbia Press.

Turetsky, M. R., Abbott, B. W., Jones, M. C., Anthony, K. W., Olefeldt, D., Schuur, E. A. G., et al. (2019). Permafrost collapse is accelerating carbon release. *Nature*, *569*(7754), 32–34. https://doi.org/10.1038/d41586-019-01313-4

Turetsky, M. R., Abbott, B. W., Jones, M. C., Anthony, K. W., Olefeldt, D., Schuur, E. A. G., et al. (2020). Carbon release through abrupt permafrost thaw. *Nature Geoscience*, *13*(2), 138–143. https://doi.org/10.1038/s41561-019-0526-0

van der Sluis, A., & van der Vorst, H. A. (1987). Numerical solution of large sparse linear algebraic systems arising from tomographic problems. In G. Nolet (Ed.), *Seismic tomography* (pp. 49–83). Reidel Publishing Co. https://doi.org/10.1007/978-94-009-3899-1_3

Vidale, J. (1988). Finite-difference calculation of travel times. *Bulletin of the Seismological Society of America*, *78*, 2062–2076.

Vidale, J. E. (1990). Finite-difference calculation of traveltimes in three dimensions. *Geophysics*, *55*, 521–526. https://doi.org/10.1190/1.1442863

Vieira, G., Hauck, C., Gruber, S., Blanco, J., & Ramos, M. (2008). *Massive ice detection using electrical tomography resistivity. Examples from livingston and deception islands*. Maritime Antarctic. 6ª Assembleia Luso Espanhola de Geodesia e Geofísica.

Walter Anthony, K. M., Anthony, P., Grosse, G., & Chanton, J. (2012). Geologic methane seeps along boundaries of Arctic permafrost thaw and melting glaciers. *Nature Geoscience*, *5*(6), 419–426. https://doi.org/10.1038/ngeo1480

Westoby, M. J., Brasington, J., Glasser, N. F., Hambrey, M. J., & Reynolds, J. M. (2012). "Structure-from-Motion" photogrammetry: A low-cost, effective tool for geoscience applications. *Geomorphology*, *179*, 300–314. https://doi.org/10.1016/j.geomorph.2012.08.021

Wolfe, S. A., Stevens, C. W., Gaanderse, A. J., & Oldenborger, G. A. (2014). Lithalsa distribution, morphology and landscape associations in the Great Slave Lowland, Northwest Territories, Canada. *Geomorphology*, *204*, 302–313. https://doi.org/10.1016/j.geomorph.2013.08.014

Yoshikawa, K. (1993). Notes on open-system pingo ice, Adventdalen, Spitsbergen. *Permafrost and Periglacial Processes*, *4*, 327–334. https://doi.org/10.1002/ppp.3430040405

Yoshikawa, K., & Harada, K. (1995). Observations on nearshore pingo growth, Adventdalen, Spitsbergen. *Permafrost and Periglacial Processes*, *6*, 361–372. https://doi.org/10.1002/ppp.3430060407

Yoshikawa, K., Leuschen, C., Ikeda, A., Harada, K., Gogineni, P., Hoekstra, P., et al. (2006). Comparison of geophysical investigations for detection of massive ground ice (pingo ice). *Journal of Geophysical Research*, *111*(E6), E06S19. https://doi.org/10.1029/2005je002573

Yoshikawa, K., & Nakamura, T. (1996). Pingo growth ages in the delta area, Adventdalen, Spitsbergen. *Polar Record*, *32*(183), 347–352. https://doi.org/10.1017/s0032247400067565

You, Y., Yu, Q., Pan, X., Wang, X., & Guo, L. (2013). Application of electrical resistivity tomography in investigating depth of permafrost base and permafrost structure in Tibetan Plateau. *Cold Regions Science and Technology*, *87*, 19–26. https://doi.org/10.1016/j.coldregions.2012.11.004

Zimmerman, R. W., & King, M. S. (1986). The effect of the extent of freezing on seismic velocities in unconsolidated permafrost. *Geophysics*, *51*(6), 1285–1290. https://doi.org/10.1190/1.1442181